Materials Characterization 200 (2023) 112832

Contents lists available at ScienceDirect

Materials Characterization

journal homepage: www.elsevier.com/locate/matchar

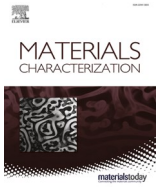

Sigma phase formation kinetics in hyper duplex stainless steel welding filler metal

Andres Acuna, Antonio J. Ramirez *

Ohio State University, Materials Science, Welding Engineering Program, Columbus, OH, United States of America

ARTICLE INFO

Keywords:
Phase transformations
Precipitation
Intermetallic phases
Nucleation
Diffusion-controlled growth
Avrami's exponent
JMAK
CALPHAD
Classical nucleation theory
Interfacial energy

ABSTRACT

This work presents a kinetic study of the sigma phase formation in hyper duplex stainless steel filler metal. Two sigma phase precipitation kinetics models were developed and compared. Initially, experimental sigma phase precipitation was built using isothermal heat treatments with durations from 30 s to 600 s, and temperatures between 600 °C and 1100 °C performed using a physical simulator. In these experiments, up to 70% of the equilibrium volumetric fraction of the sigma phase was achieved in 600 s. A CALPHAD-based kinetic model was developed using the experimental transformation data. Constant cooling rate conditions were calculated using the CALPHAD-based model revealing a minimum cooling rate of 4 °C/s as the threshold for the sigma phase to form. The microstructure evolution of the sigma phase precipitation follows the known eutectoid decomposition mechanism of ferrite transformation to sigma phase and secondary austenite ($\alpha \rightarrow \sigma + \gamma_2$), which evolved at the latter stages of the precipitation times, the lamellar σ/γ_2 morphology results from the eutectoid reaction, which is diffusion controlled. Finally, we applied the JMAK kinetic law to model the sigma phase formation on both datasets, the experimental and the CALPHAD-based TTTs. In the JMAK linearized plots, a kinetic mechanism change was found, switching from an eutectoid decomposition stage to a diffusion-controlled growth stage. While the JMAK calculations provided good agreement with the experimental data, the CALPHAD-based data only agreed near the maximum kinetics temperatures between 900 °C and 925 °C. Nevertheless, the sigma phase transformation kinetics modeled using JMAK equations properly described the experimental data describing its double kinetics behavior and reproduced the CALPHAD-based TTT at the maximum kinetics temperature range.

1. Introduction

Duplex stainless steels are widely used due to their excellent combination of corrosion resistance, toughness, and strength. The best corrosion and mechanical performance are delivered by the recently developed sub-family known as hyper duplex stainless steel HDSS which has a PREn [1–3] higher than 48 [4]. However, the widespread use of this material could bear challenges due to their expected propensity to the formation of unwanted and severely damaging intermetallic phase precipitation during manufacturing operations like welding.

The corrosion resistance, toughness, and strength come from the specific chemical composition designed to produce optimal microstructure, a 50–50 ferrite-austenite system. However, alloying makes the material susceptible to intermetallic and nitride precipitation when exposed to temperatures between 600 °C to 1100°C [5]. The Sigma phase is the predominant precipitate in the highly alloyed DSS. It nucleates at interfaces and grain edges and grows into the ferrite consuming Cr and Mo from the BCC structure. As a consequence, the Cr and Mo-depleted neighboring phases have reduced corrosion resistance [6–8]. At the same time, the sigma phase ordered tetragonal crystallographic structure has very low dislocation mobility, reducing the toughness [9–11].

Obtaining a sigma-free processed material is critical for most applications. Therefore, the success of the HDSS implementation relies on the understanding and control of the sigma phase and other intermetallic phases formation. Hence, this study presents an in-depth sigma kinetics analysis of the 2707 HDSS material used to produce the filler metal for welding. Sigma phase formation as a function of temperature and time has been described using the Johnson-Mehl-Avrami-Kolmogorov - JMAK [12–16] kinetic calculation Eq. (1).

$$f = 1 - e^{(-kt^n)} \tag{1}$$

where f is the transformed sigma volume fraction ($0 < f < 1$), t is the

* Corresponding author.
E-mail address: ramirez.49@osu.edu (A.J. Ramirez).

https://doi.org/10.1016/j.matchar.2023.112832
Received 10 November 2022; Received in revised form 8 March 2023; Accepted 19 March 2023
Available online 29 March 2023

transformation time, n is the Avrami's exponent related to the rate of nucleation and growth, and k is related to the energy barrier for the sigma phase formation. This coefficient k can also be described as an Arrhenius equation, as shown in Eq. (2). Where k_0 is a pre-exponential constant, Q_σ is the activation energy for sigma phase formation for nucleation and growth, T is the temperature in Kelvin, and R is the gas constant.

$$k = k_0\, e^{\left(-\frac{Q_\sigma}{RT}\right)} \tag{2}$$

Eq. (1) can be linearized using its logarithm form, yielding a linear (y = ax + b) equation:

$$ln(-ln(1-f)) = n(ln(t)) + ln(k) \tag{3}$$

A JMAK double kinetics mechanism, nucleation, and initial growth followed by diffusional growth were seen reproducing the sigma phase formation seen by Elmer et al. [17] using in-situ X-ray diffraction on 2205 DSS and dos Santos et al. [18] in a UNS S31803 up to 900 °C. Marques et al. [19] also found a double kinetics mechanism attributing it to a chi-phase assisted nucleation followed by sigma phase growth.

The HDSS was developed for heat exchanger applications [20] mainly as tubes. For this application, a similar specification filler metal was developed for the tube-to-tube welds, cladding of the carbon steel tubesheet, and for tube-to-tubesheet welds. Most of the research developed addressed only the tube material and focused on the corrosion performance. Chemical composition additions of Cu [21,22], W [23], and Ce [24,25] in small ingots were analyzed by Jeon et al. [21–23,26] and Kim et al. [25] they found a sigma phase formation reduction from Ce additions whereas W and Cu could hinder sigma phase formation at the expense of an increase of chi phase precipitation. Zhang et al. [27] investigated the sigma phase precipitation behavior of a 25 kg heat rolled to a 4 mm thick plate. He experimentally calculated a TTT and defined the nose temperature at 950 °C while also strong eutectoid decomposition ($\sigma + \gamma_2$) after 30 min of aging.

There was little research aiming for the sigma phase formation. Also, no study was found addressing sigma phase kinetics on the HDSS wire. More critically, in the aimed applications, the filler metal wire is deposited causing solidification and experiencing multiple thermal cycles. Therefore, this investigation aims to evaluate sigma phase kinetics in the HDSS filler metal through analytical calculations based on experimental and CALPHAD-based data. Since sigma phase presence is very detrimental, investigating its formation kinetics is critical to ensure that the HDSS can be processed while avoiding such damaging intermetallic phase presence.

2. Materials and methods

The HDSS material in its welding filler metal 27.7.5.L form is used for this study. Specifically, pre-drawn wire of 5.6 mm diameter (outer). Table 1 presents the material's chemical composition measured using optical emission spectroscopy (OES) SpectroMax. In addition, the nitrogen was also quantified using a combustion spectrometer Leco TC600. In its solubilized form, intermetallic phases were not found through optical and Scanning Electron Microscopy – SEM analysis.

3. Precipitation heat treatment

An experimental precipitation map is developed utilizing a Gleeble 3800 physical simulator. As presented in Fig. 1 (a), heat treatment of each 5.6 mm × 80 mm specimen is performed at 100 °C/s heating until reaching a defined isothermal aging temperature. The temperature is held for the specified dwell time, followed by cooling at 37 °C/s. Each rod specimen utilizes three type K thermocouples attached across a 20 mm free span, Fig. 1 (b). The control thermocouple is located at the specimen (T0). Additionally, two other thermocouples are separated by 5 mm (T5) and 8 mm (T8) in longitudinally opposite directions of T0 Fig. 1 (c). The two additional thermocouples revealed peak temperatures T5 as 90% ±0.018% and T8 as 72% ±0.004% of the set control temperature at T0.

After the heat treatments, all the samples were sectioned longitudinally for microstructural characterization. The time and temperature data combined with the intermetallic volume fraction populated the experimental kinetics time-temperature-transformation TTT contour plot. In this map, the data was interpolated using the kriging [28] method, and the isovolumetric lines represent the interpolated kinetic TTT curves. This experimental data was used for the JMAK kinetics analytical calculations from 775 °C to 1000 °C and it is applied to develop the CALPHAD-based kinetics model.

4. Microscopic characterization

Quantitative metallography uses a combination of optical (Olympus DP2-BSW microscope) and electron (FEI Apreo LoVac High Resolution) microscopy to quantify the intermetallic volume fractions. The samples were prepared by grinding using 240 up to 1200 grit, 1 μm diamond paste polishing, and finally, a 0.02 μm colloidal silica polishing for 3 h.

The microstructural etching process applies a dual-step electrolytic etching solution of 40% HNO_3 + 60% distilled water, an adaption of the etching developed by Ramirez et al. [29,30] using the steps:

A) 1.3 V for 20 s for interphase etching.
B) 0.9 V for 50–60 s for preferential ferrite etching.

This etchant is specifically selected to reveal the intermetallic properties(white) and provide a contrast distinction between the ferrite (brown/caramel) and austenite (tan/yellow) constituents (Fig. 3).

Phase fraction quantification is obtained through digital image analysis via light optical microscopy (LOM) and scanning electron microscopy (SEM) applications. In this analysis, the gray-scale images are filtered through a range threshold for selecting and quantifying ferrite, austenite, chi phase, and sigma phase. The volume fraction data presented are average values of five images randomly taken at 1000× magnification.

5. Kinetic law calculations

The Johnson-Mehl-Avrami-Kolmogorov JMAK kinetic [17,18,25,31–35] Eq. (1) is used to describe sigma phase formation kinetics. Through this analytical method, experimental precipitation data is taken in 25 °C steps between 775 °C to 1000 °C. The data from Eq. (3) generate linearized (ln(−ln(1-f) x ln(t)) plots that graphically describe sigma phase formation. From the linearized plots, Avrami's exponent n and time activation k are extracted. The linearized plots depend only on the temperature, time, and phase volume fraction data. A comparison is established between the JMAK calculations using the experimental and the CALPHAD-calculated precipitation data.

Table 1
Measured chemical composition in wt% for the rod samples used in physical simulation and the CALPHAD-based kinetic model. The PREn formulation used is the same as the API 582 Standard4, PREn = (%Cr + 3.3% Mo + 16 %N).

Material	Fe	C	Cr	Ni	Mo	N	Co	Mn	PREn [4]
Rod – 27.7.5.L	Bal.	0.02	25.56	6.31	4.74	0.4	1.32	0.96	47.9

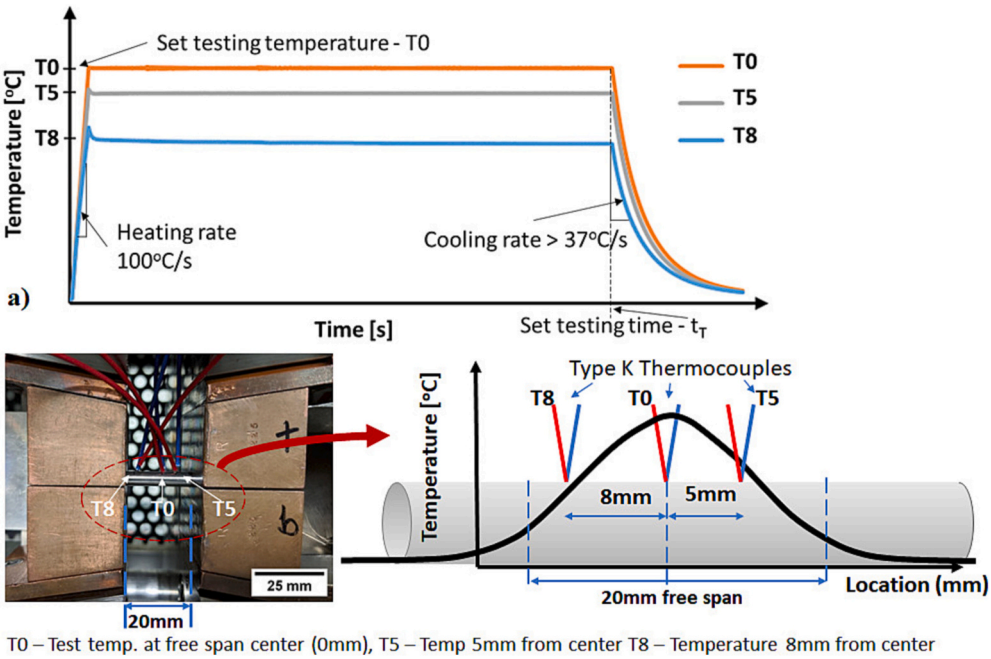

Fig. 1. Precipitation testing (a) Schematic of the applied aging thermal history. (b) a specimen on the testing chamber showing the three type k thermocouples attached to it within the 20 mm free span. (c) schematic of physical simulation rod specimen and temperature distribution, testing temperature control at T0, T5 = 0.9*T0, and T8 = 0.72*T0.

6. CALPHAD modeling and validation

The CALPHAD program used refers to experimental thermodynamic databases (TCFE11 and MOBFE6) to fit the minimization of the Gibbs energy for the more stable phase considered. Those phase diagrams calculate the stability of the expected phases in thermodynamic equilibrium conditions as a function of temperature and individual elements content. The phases: ferrite, austenite, sigma, chi, nitrides (Cr_2N), and liquid from the software thermodynamics database (TCFE11) serve as input conditions to the model.

Nonequilibrium, CALPHAD-based calculations are used to develop sigma phase precipitation time-temperature-transformation (TTT) curves. The CALPHAD-based kinetics uses the classical nucleation theory [36,37] to model nucleation on a multi-component system. The nucleation process can be described as a multiple-step transformation:

I. Incubation Time $\boldsymbol{\tau}$: time consumed to the steady state nucleation conditions be established, no nucleation occurs,
II. Steady State ($\boldsymbol{J_s}$): in this step, the nucleation rate increases linearly with time increment.
III. Nucleation rate decrease: particle growth decreases the supersaturation causing the nucleation to decrease.
IV. Ostwald ripening: competitive growth where extensive particles grow at the expense of the smaller and less stable ones.

The classical nucleation theory has its central problem on the nucleation rate [38] Eq. (3).

$$\boldsymbol{J(t) = J_s e^{(-\tau/t)}} \tag{4}$$

This nucleation rate depends on the incubation time $\boldsymbol{\tau}$ and the steady state nucleation rate $\boldsymbol{J_s}$ Eq. (4):

$$\boldsymbol{J_s = Z\beta^* N_o e^{\left(-\frac{\Delta G^*}{kT}\right)}} \tag{5}$$

where **Z** is the Zeldovich factor, which considers the probability that a nucleus at the top of the barrier will continue to form the new phase rather than dissolve. It is related to the thermodynamics of the nucleation process and is dependent on the interfacial energy and nucleus critical radius size.

$\boldsymbol{\beta^*}$is the atomic or molecular attachment rate, describing the Kinetics of mass transport in the nucleation process.

$\boldsymbol{N_o}$ is the available nucleation site density.

$\boldsymbol{\Delta G^*}$is the critical nucleus formation Gibbs energy.

During solidification, the homogeneous nucleation free energy change accounts for three contributions:

At the temperature at a new phase is stable, the creation of a new volume V causes a volume free energy reduction $\boldsymbol{V\Delta G_v}$.

The creation of an interface area A causes a free energy increase, proportional to the two phases' interfacial energy, $\boldsymbol{A\gamma}$.

The new transformed volume V gives rise to a misfit strain energy $\boldsymbol{V\Delta G_s}$.

However, heterogeneous nucleation is typical nucleation for solids, especially weld/cladding processes. In heterogeneous nucleation, there are nucleation sites that are non-equilibrium defects, such as vacancies, inclusions, grain boundaries, and interfaces. In these cases, the creation of a new nucleus causes the destruction of a defect ($\boldsymbol{\Delta G_d}$) reducing the energy barrier. Hence, the heterogenous nucleation Gibbs energy change becomes: $\boldsymbol{\Delta G = -V\Delta G_v + A\gamma + V\Delta G_s + \Delta G_d}$:

This model is controlled primarily through nucleation site distribution $\boldsymbol{N_o}$ which increases the nucleation rate and the nucleation barriers inside $\boldsymbol{\Delta G}$. From the energy barrier parameters, the model was more sensitive to the interfacial energy $\boldsymbol{\gamma}$. These parameters pair, $\boldsymbol{N_o}$ and $\boldsymbol{\gamma}$, are also used to adjust the model based on developing experimental data, as shown by Acuna et al. [39]

Additive rule calculations are used to build continuous cooling transformation (CCT) curves derived from the modeled TTT curves. Three critical cooling rates, 1 °C/s, 2.5 °C/s, and 4 °C/s, have been applied to the sample rods on the physical simulator to validate the referenced model.

7. Results and discussion

7.1. CALPHAD equilibrium calculations

The thermodynamic equilibrium calculations are developed based on the chemical composition, Table 1. From the thermodynamics calculations, a section of the isopleth diagram as a function of nitrogen is presented in Fig. 2 – CALPHAD equilibrium calculation (TCFE11 database), phases volumetric fraction as a function of temperature.Fig. 2 at the measured nitrogen content of 0.4.

Fig. 2 shows the equilibrium predicted phase volume fractions as a function of temperature. This alloy solidification follows the microstructure evolution as $\mathbf{L} \rightarrow \mathbf{L} + \boldsymbol{\alpha} \rightarrow \mathbf{L} + \boldsymbol{\alpha} + \boldsymbol{\gamma} \rightarrow \boldsymbol{\alpha} + \boldsymbol{\gamma}$, with the austenite only forming at the last state of the s solidification, similar to the SDSS [29]. Austenite becomes stable below 1365 °C while the liquid phase is still present. The austenite presence during the solidification hinders ferrite grain growth. In addition, the stabilization of austenite at this high temperature is mainly due to the high content of austenite promoters such as N and Ni. During cooling, the austenite content continuously increases in solid-state, reaching the ideal 50% ratio at 1165 °C.

The sigma phase is stable below 1105 °C*. sigma* phase and austenite fraction increase rapidly with temperature reduction, consuming the remaining ferrite to the point of BCC phase absence below 1050 °C under equilibrium conditions. At lower temperatures, the sigma phase equilibrium volume fraction reaches 40% at 800 °C. Below this temperature, the chi phase also becomes stable, reaching a maximum of 19% volume fraction at 550 °C at the expense of the sigma phase.

The equilibrium volumetric phase distribution of maximum sigma phase content proves to be consistent with similar simulations referenced in studies of SDSS [9,30,40–42], and DSS [30]. The duplex $\alpha + \gamma$ microstructure is mostly ferrite, with the austenite forming in the solid state. Ferrite has a higher Cr and Mo solubility than austenite. In addition, these elements also have higher diffusivity coefficients in the BCC lattice. Hence, sigma as a chromium and molybdenum-rich phase is more dependent on the ferrite volume fraction for nucleation and growth.

The DSSs have two main factors limiting the ferrite volume fraction and grain size: the austenite forming during the solidification and the solid-state ferrite-to-austenite transformation. The austenite stability is mostly dictated by the alloying of nitrogen and nickel. Zhang et al. [43] modeled the austenite-to-ferrite transformation on 2205 DSS during welding cycles as a function of nitrogen diffusion and found that a non-uniform austenite-ferrite starting structure delays the transformation towards the end, taking at least 30% more time to complete the $\gamma \rightarrow \alpha$ transformation.

The HDSS steel has an exceptionally high nitrogen content (0.4 wt %), being a less costly [44] gamma stabilizer than Ni, which also improves austenite stabilization and localized corrosion resistance and mechanical strength. However, the nitrogen alloying content is reduced during welding due to its limited solubility in the liquid metal [40,45]. Hence the usual requirement for nitrogen additions on the welding shielding gas for all DSS, including the HDSS.

8. Microstructural characterization

Quantitative metallography on the pre-drawn HDSS rods revealed the solubilized condition with ferrite volume fractions of 49.5% ± 0.3%, as shown in Fig. 1 (a). From EBSD measurements Fig. 1 (b), the ferrite grain size has an area of 64.61 μm^2 ± 25.42 μm^2 while the austenite grains have an average area of 80.16 μm^2 ± 34.15 μm^2.

Table 2 presents all the applied heat treatments combined with the respective sigma phase volumetric fractions. It is critical to note that the zero values are actual measures of data obtained at the T8 location. The

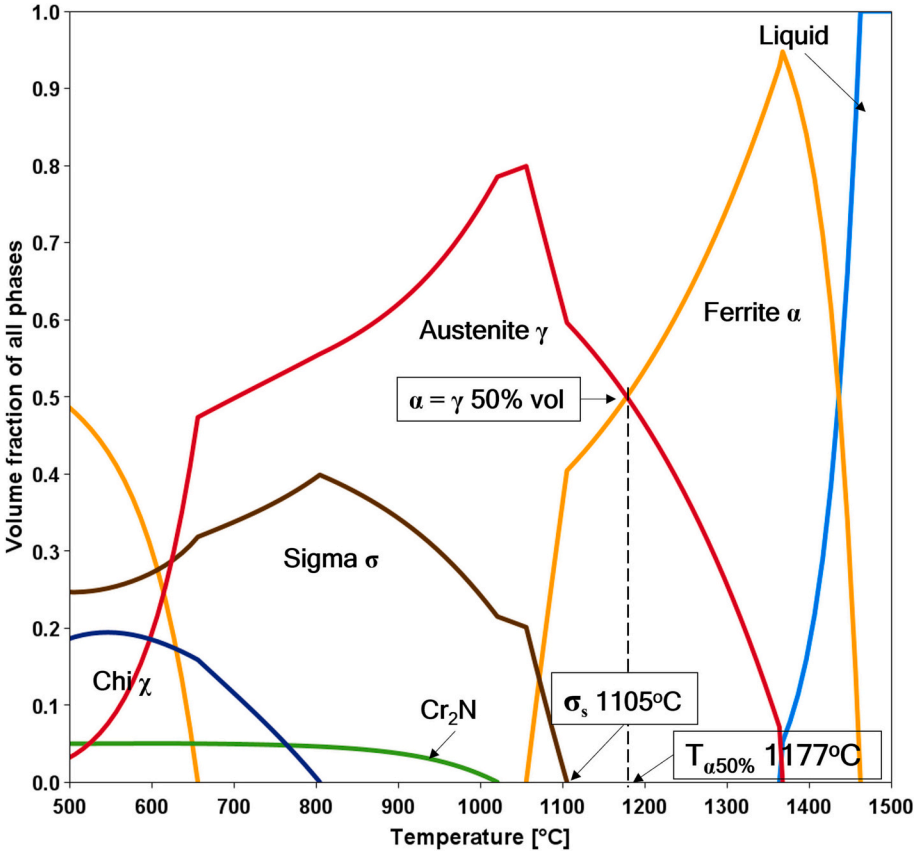

Fig. 2. CALPHAD equilibrium calculation (TCFE11 database), phases volumetric fraction as a function of temperature.

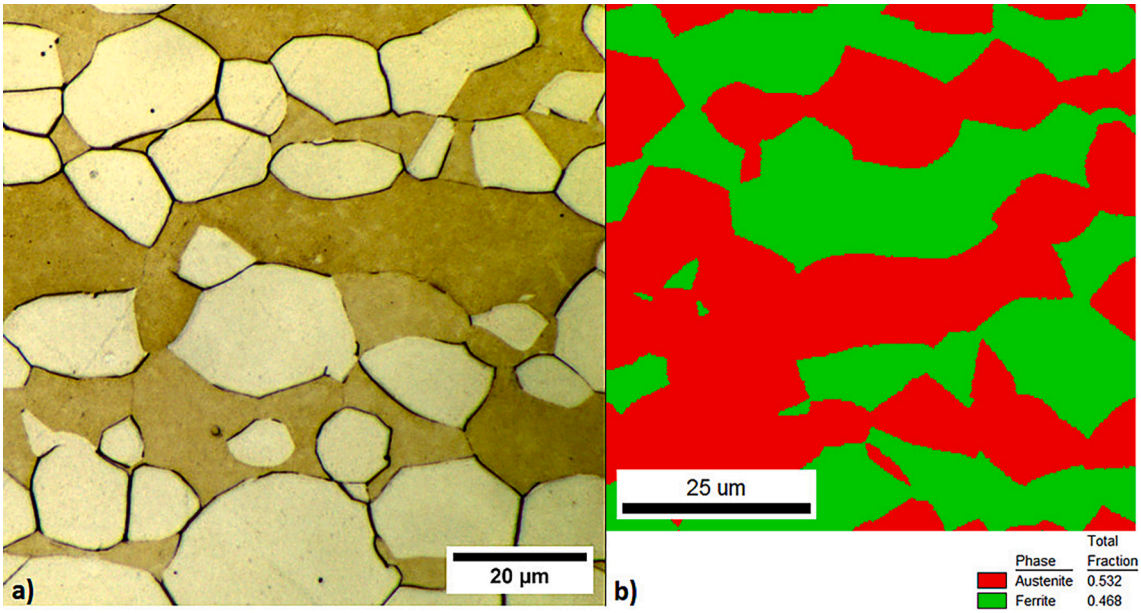

Fig. 3. HDSS rod specimen solubilized microstructure, experimental physical simulations initial microstructure. Optical microscopy on the etched sample, austenite, and ferrite microstructure (a). SEM EBSD measurements data of phase distribution.

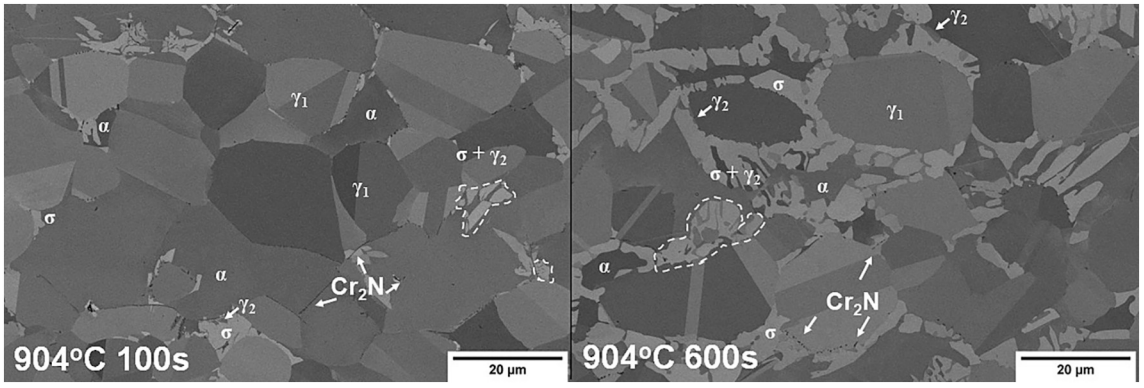

Fig. 4. Microstructural comparison of HDSS isothermally heat-treated samples at 904 °C. (a) heat treated for 100 s, presenting interfacial nuclei and sigma phase precipitates growth with secondary austenite formation. (b) heat treated for 600 s with extensive sigma phase precipitates growth at the expense of ferrite. In-column detector, backscattered electrons image SEM.

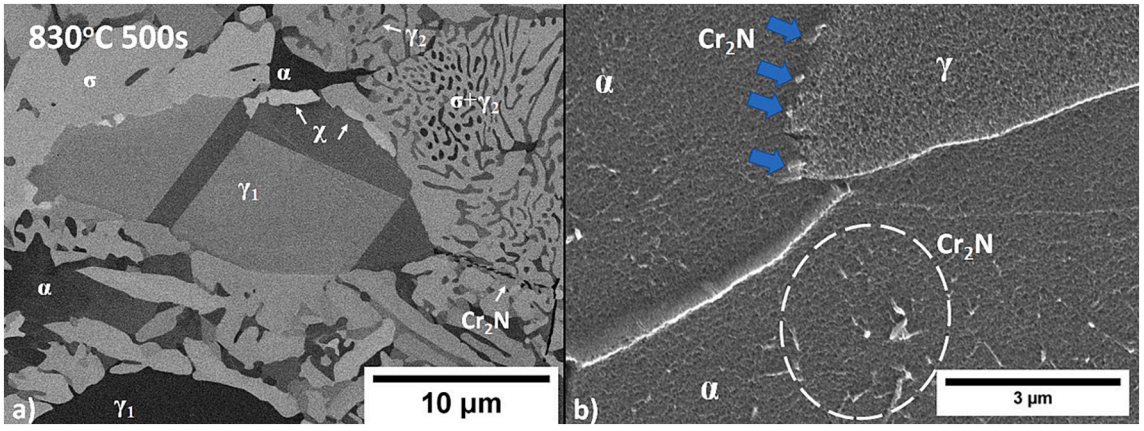

Fig. 5. (a) Multiple sigma phase morphologies found in the sample treated at 830 °C for 500 s. Large blocky grains at the top left, lamellar σ + γ_2 structure at the top right, and eutectoid decomposition at the bottom. SEM: in-column detector, backscattered electrons. (b) Ferrite intragranular Cr_2N precipitation (blue arrows). SEM: in-column detector, secondary electrons. (For interpretation of the references to colour in this figure legend, the reader is referred to the web version of this article.)

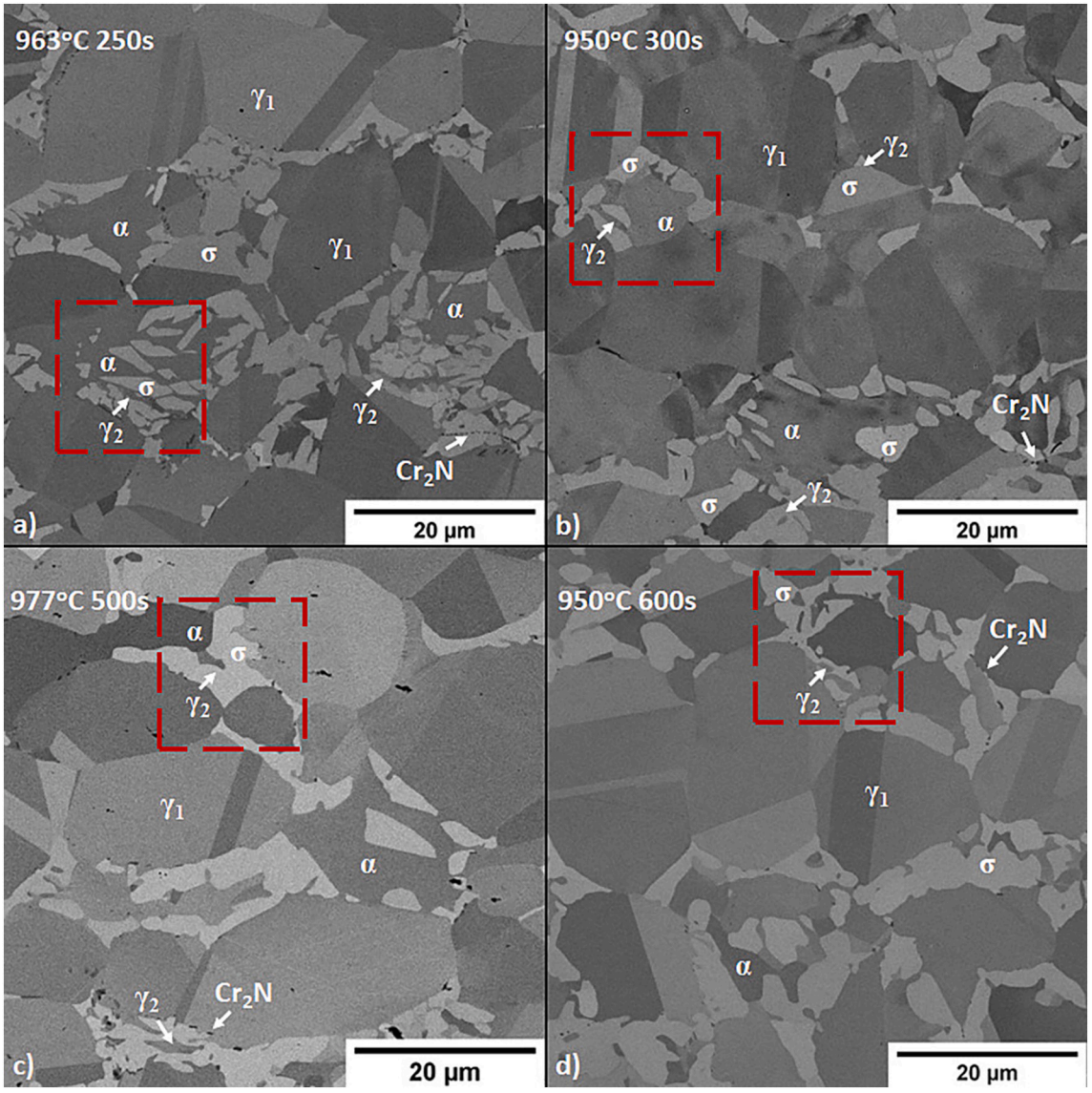

Fig. 6. Sigma phase growth close to 950 °C for (a) 250 s, (b) 300 s, (c) 500 s, and (d) 600 s. Sigma growth caused clear ferrite consumption changing its morphology from cellular structure to large and coalesced grains. In-column detector, backscattered electrons image SEM.

zero volumetric fractions were found more frequently on T8 due to its extended distance from the temperature-controlled position (T0), which in some cases was below the sigma precipitation temperature range.

Fig. 4 presents backscattered electrons SEM images of the microstructure formed at 900 °C for 100 s (a) and 900 °C for 600 s (b). In the 100 s specimen, blocky sigma phase grains grow while consuming part of the ferrite. In addition, small sigma interfacial nuclei are present, and some cells of $\sigma + \gamma_2$ clusters begin to appear (dashed white line), forming a total sigma phase volume fraction of 3.64% ±0.68%. When treating the alloy at a similar temperature (904 °C for 600 s), the sigma phase fraction reached 27.6% ±2.09%, corresponding to 70% of the predicted equilibrium state volumetric fraction.

Interestingly, the known sigma/secondary austenite lamellar structure resulting from the eutectoid ferrite decomposition $\alpha \rightarrow \sigma + \gamma_2$ is not often seen at heat treatment times up to 100 s [31]. In fact, the $\sigma + \gamma_2$ lamellar structure was mostly seen on samples heat treated for longer than 200 s, whereas the shorter time heat treatment produced blocky sigma phase grains with some secondary austenite in between. In comparison, the sample heat-treated at 830 °C for 500 s (Fig. 5 a) presents a combination of both mentioned sigma morphologies, large σ plates with small γ_2 on the top left side and the cellular $\sigma + \gamma_2$ structure on the top right. On both sides of the image, the primary ferrite grain is almost completely consumed. Conversely, where the sigma phase grains impinged each other, ferrite is still present, as seen at the bottom of the image.

Fig. 5 (b) presents ferrite intragranular Cr_2N colony precipitation, white dashed ellipsis. Also, intergranular Cr_2N, blue arrows, are seen at the α/γ interface and previous ferrite grain boundaries. Because Fig. 5 (b) is a secondary electron image of an etched sample, the topography is highlighted, and the edges appear brighter in the image.

Fig. 6 presents microstructural backscattered electrons SEM images of the specimens heat-treated at approximately 950 °C for 250 s, 300 s, 500, and 600 s. In this image, the increasing time reveals the continuous growth of the sigma phase progressively consuming the ferrite. The impingement of growing sigma phase grains caused the trapping of small secondary austenite grains shown in the red dashed box of each image.

Interestingly, the large previous ferrite grains consumed by the cellular $\sigma + \gamma_2$ structure resulting from the eutectoid decomposition were seen in the samples treated for 600 s at 904 °C, 858 °C, and 842 °C. On the other hand, above 950 °C, only a small number of cellular structures were found, and blocky sigma phase grains were more

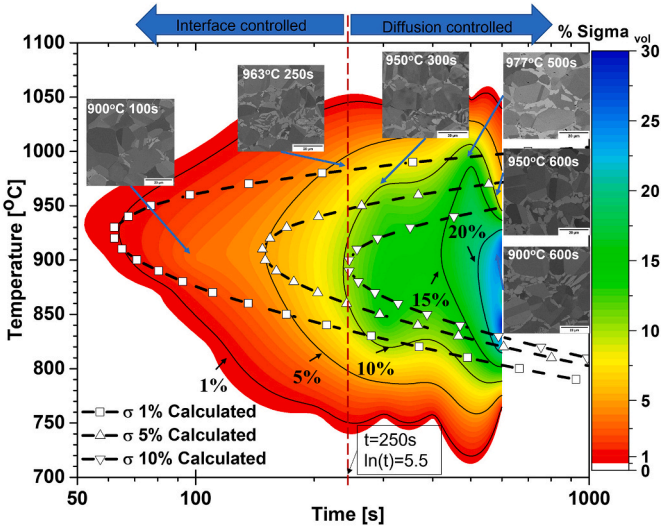

Fig. 7. Sigma phase interpolated experimental TTT map presenting the microstructures of Figs. 4 and 6 overlayed on their corresponding time and temperature. Sigma phase CALPHAD-based calculated TTT curves and symbol lines were overlayed on the experimental map. The dashed red line at $t = 250$ s reveals the time at JMAK calculations found the sima phase kinetics formation mechanism changing from interfacial controlled to diffusion-controlled growth. (For interpretation of the references to colour in this figure legend, the reader is referred to the web version of this article.)

common for the same treatment time. The morphological difference is directly related to the eutectoid decomposition, which relies upon lateral diffusion of a solute along a sweeping grain boundary [36]. In this case, the solute diffusion along the grain boundary to a solute sink, such as the sigma phase precipitates, causes the boundary to move. However, at higher temperatures, the low undercooling hinders the nucleation. Therefore, fewer solute sinks are available to cause boundary movement. Conversely, at higher undercooling, the high nucleation rate provides multiple solute sinks (sigma phase nuclei) to cause boundary movement. Accordingly, with the higher precipitate volume, higher boundary movement occurs causing faster cellular colonies growth.

The small dark precipitates are chromium nitrides - Cr_2N [17,18,29], were seen in all heat treatments at the α/γ and the σ/ γ interfaces, Fig. 6 (a), (b), and (c). These precipitates appear dark in the backscattered electrons image due to their lower backscatter coefficients, in particular, N with low atomic numbers.

Fig. 7 presents the sigma phase TTT experimental map with the microstructures shown in Figs. 4 and 6 overlayed in its corresponding volumetric fraction. This map is an interpolated contour plot of the quantified sigma volume fraction from 0.5% up to 30% as a function of the heat treatment temperature and time. Due to the interpolation method [28], some oscillations can be seen in the contour lines, in particular for longer times. Nevertheless, the continuous black lines are experimental interpolated TTT curves. The red dashed line marks the 250 s, the time when the linearized kinetics law plots revealed a change in the kinetics transformation mechanism, which we will discuss further.

9. Precipitation kinetics analysis

Multiple authors [17,18,25,31–35] have used the Johnson-Mehl-Avrami-Kolmogorov JMAK kinetic analytical calculations, Eq. (1), to describe the sigma phase kinetics in other alloys. The Avrami's exponent n and time activation pre-exponent k can be graphically calculated using its linearized form Eq. (3).

For this study, we apply these analytical calculations to describe

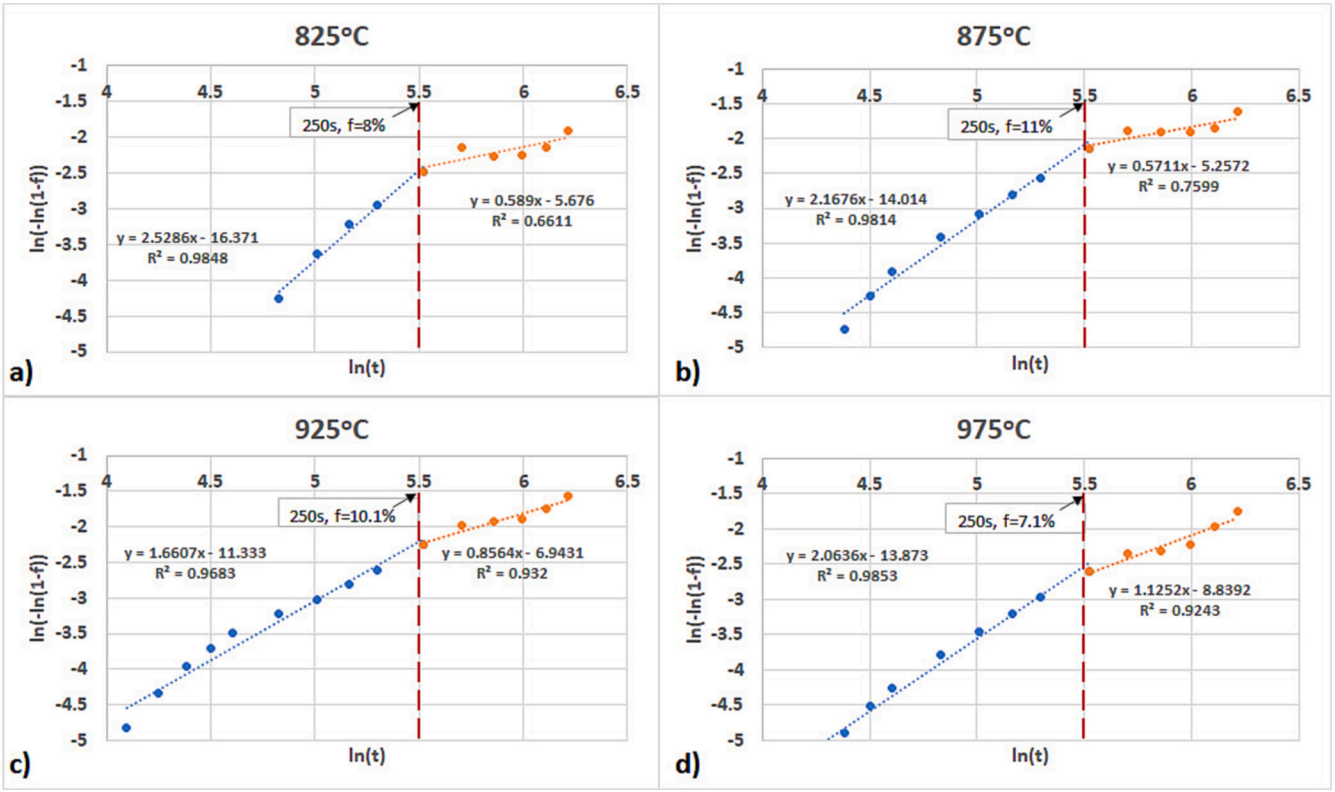

Fig. 8. Kinetic law linearized plots at 825 °C (a), 875 °C (b), 925 °C (c), and 975 °C (d). The change of slope at ln(t) = 5.5 (250 s) suggests a change in the kinetic mechanism. From 0 to 250 s, the transformation occurs by eutectoid decomposition and interface-controlled growth. After 250 s, the phase transformation proceeds by diffusion-controlled growth.

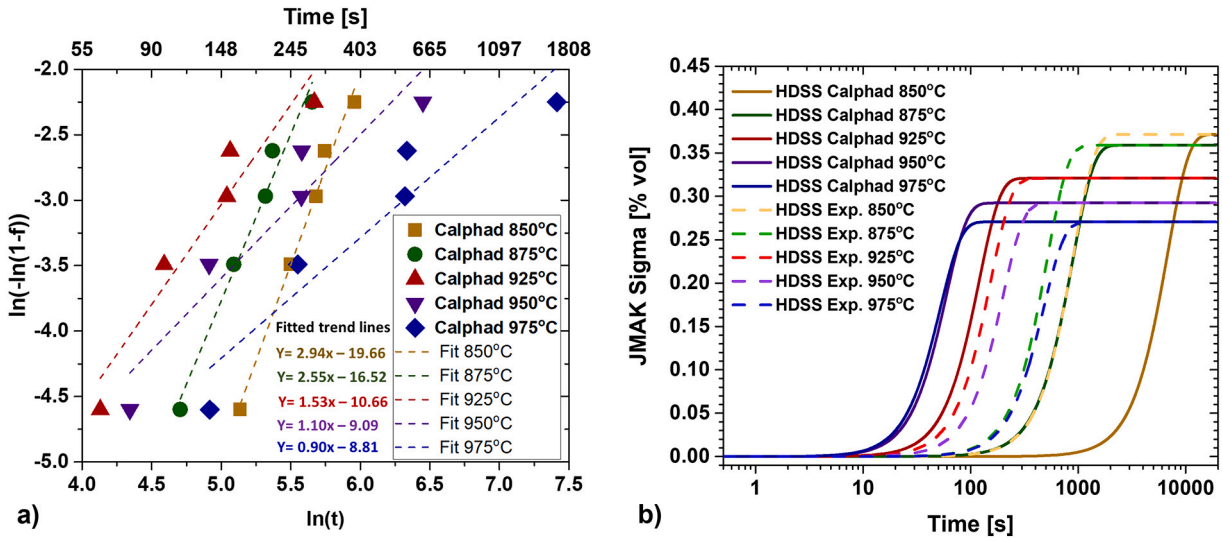

Fig. 9. – (a) Sigma phase JMAK Kinetics linearized plot from the CALPHAD-based TTTs data. Linear regressions presented at 850 °C, 875 °C, 925 °C, 950 °C. and 975 °C. (b) Sigma phase JMAK kinetics sigmoidal curves of CALPHAD-based calculations (solid lines) and experimental data (dashed lines). Yellow lines at 850 °C, green at 875 °C, red at 925 °C, magenta at 950 °C, and blue at 975 °C. (For interpretation of the references to colour in this figure legend, the reader is referred to the web version of this article.)

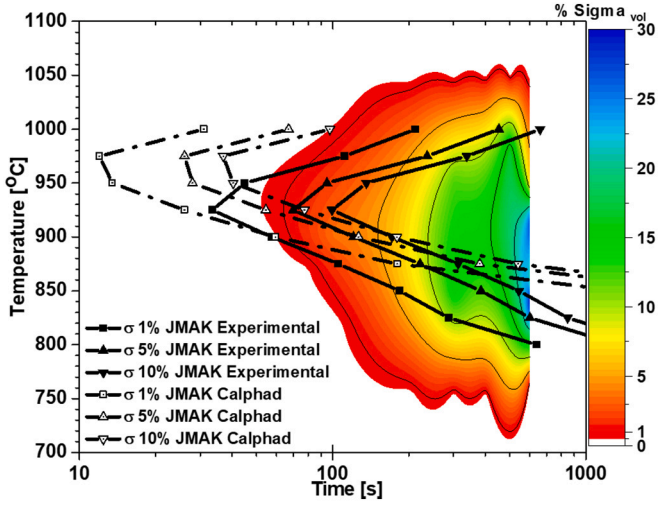

Fig. 10. Sigma phase JMAK kinetics calculated TTTs of CALPHAD-based calculations (dashed-dot lines) and experimental data (solid + symbol lines) overlayed on the interpolated experimental TTT map. 1% of sigma phase at maximum kinetics temperature range formed in 10.5 s (JMAK using CALPHAD data), 30.5 s (JMAK using experimental data), and 62.2 s experimental data.

sigma phase kinetics formation on HDSS welding filler metal. The calculations used the experimental TTT map data from 775 °C to 1000 °C in 25 °C steps increments at the times of 60, 70, 80, 90, 100, 125, 150, 175, 200, 250, 300, 350, 400, 450, and 500 s. Some of the linearized plots, ln (−ln(1-f)) as a function of ln(t), are presented in Fig. 8, where *n* and *k* were calculated at each temperature.

A change of slope was seen occurring consistently at 250 s or ln(t) = 5.5. This slope change suggests a change in the sigma phase kinetics mechanism. Therefore, the data was separated into two linear stages: a first slope, steeper *n*, considered until 250 s, and a second slope, smaller *n*, between 250 s and 500 s. Each regression slope (Eq. (3)) corresponds to an average *n* Avrami exponent. The exponent change corresponds to a change in the kinetics mechanism, also reported in the literature [17–19,46]. Elmer et al. [17] Dos Santos et al. [18] and Da Fonseca et al. [46] identified double kinetics as an initial stage of eutectoid decomposition or interface-controlled growth followed by the second stage of diffusion growth in DSS and SDSS. Marques et al. [19] associated the first kinetic stage strongly as influenced by the Chi phase acting as a sigma phase nucleation site. In contrast, the second stage was a diffusion growth into the ferrite matrix.

Christian [47] stated that *n* between 1 and 4 indicates a transformation process related to eutectoid decomposition and interface-controlled growth. When the exponent is between 0.5 and 2.5, a diffusion growth mechanism is expected.

Table 3 presents the calculated Avrami exponent *n* for each temperature in the first and second slopes. The first slope *n* values are attributed to eutectoid decomposition or interface-controlled growth. Maximum kinetics is found at the temperature range of 900 °C-950 °C, which is the nose of the c-shaped TTT curves. Interestingly, the calculated *n* values are close to 2, in the range that Christian [47] defines as the condition of grain edge nucleation after saturation. However, it is also recognized that for most transformations, *n* is somewhat independent of temperature while *k* varies markedly. Assuming that an average value of *n* can be used to describe each transformation slope, this work uses *n* as 2.25 and 0.81 for the first and second slopes, respectively.

The second slope presents values between 0.49 and 1.13 which suggests diffusional growth as thickening of needles, cylinder, and plate morphologies [47]. The values obtained in this research are a great match with other authors in duplex stainless steels [17,18].

Even though the transition of the kinetics mechanism is not time-limited, rather it is related to nucleation saturation. It was found to happen consistently at 250 s or ln(t) = 5.5, as shown by the red dashed line in Fig. 7 and Fig. 8. The change of diffusion-controlled growth explains the cellular morphology ($\alpha \rightarrow \sigma + \gamma_2$) formed through a cooperative partition of elements between the γ_2 and the sigma phase [17,31] through diffusion.

Furthermore, it is also noticeable that at higher temperatures, when the nucleation driving force is smaller due to the reduced undercooling and diffusion is maximized, the Avrami's exponent average is closer to 2, consistent with diffusion-controlled growth [47]. Conversely, at lower temperatures, when nucleation is dominant, and diffusion is limited, the Avrami's exponent average is 2.6, which is also consistent with Cristhian [47] description of grain edge nucleation after saturation.

The change in the sigma kinetics mechanism occurring at 250 s also agrees with the change in morphology seen before, Fig. 6. The sigma phase morphology in times until 200 s is predominantly bulky coalesced grains, whereas, after the 250 s, the lamellar structure $\sigma + \gamma_2$ is largely

Table 2
Sigma phase precipitation experimental data. HDSS filler metal isothermal physical simulation reporting sigma phase volumetric fraction, temperature, and time pair. Sigma phase quantification, measured by digital image thresholding of five SEM backscattered images.

Time	30s	50s	80s	90s	100 s	150 s	200 s	250 s	300 s	400 s	500 s	600 s
Temperature [°C]	Sigma phase volume [% vol]											
1100					0						0	0
1050							0	0	0	0	0	0
						0.38 ±						
1000		0	0			0.17		1.06 ± 0.60			0	
						1.10 ±					16.91 ±	
980				1 ± 0.17		0.35		1.58 ± 0.62			2.33	
973				1.2 ± 0.21								
963								3.74 ± 0.65				
						4.67 ±			12.08 ±			
950						2.40			1.11			6.04 ± 1.25
925												
								14.76 ±				
918								2.81				
					3.64 ±							
904		0			0.68							27.6 ± 2.09
				4.08 ±								
887				1.40								
			0.48 ±									
870			0.11									
							6.75 ±					19.45 ±
854							3.11					4.62
			0.04 ±									30.88 ±
845			0.03						14.5 ± 0.84			4.00
					0.09 ±							
815		0			0.03							
					0.15 ±							
800	0	0			0.12			0				
776					0							
750							0		0	0		0
720		0					0					
693	0											
678					0							
662											0	
642		0			0		0		0			
577	0											
565					0							
485		0										

Table 3
JMAK Avrami's exponent n calculated from the experimental data. Values presneted for the first slope (eutectoid decomposition or interface-controlled growth) and second slope (diffusion-controlled growth. Sigma phase volumetric fraction at kinetics mechanism transition.

Temperature °C	n 1st slope	n 2nd slope	Volume fraction at kinetics transition
775	2.60	0.97	3%
800	2.79	0.81	5%
825	2.53	0.60	8%
850	2.76	0.49	10%
875	2.17	0.57	11%
900	1.92	0.74	11%
925	1.66	0.86	10%
950	1.74	0.88	9%
975	2.06	1.13	7%
1000	2.23	1.09	5%
Average	2.25	0.81	
Max	2.79	1.13	
Min	1.66	0.49	

seen. That suggests that the lamellar formation from the ferrite decomposition is a diffusion-growth governed mechanism. Therefore, the sigma phase formation in the HDSS was described using two JMAK equations, where k is dependent on n and temperature, and it was calculated from the linearized plots. Table 4 presents the obtained sigma phase kinetics JMAK equation using the experimental data and CALPHAD data. The experimental data is described through two equations, one for the kinetic mechanism of nucleation and interface-controlled growth and a second equation for the kinetic mechanism of diffusion-controlled growth.

10. From the CALPHAD model to the sigma phase CCTs diagrams

The CALPHAD-based kinetics calculate the sigma phase kinetics TTTs using the classical nucleation theory. It calculates the volume of the precipitation through the nucleation rate. For that, it used thermodynamic calculation for to obtain the energy barrier, which accounted characteristics of the matrix phase, such as grain size and aspect ratio interfacial energy. Nucleation sites and interfacial energy are not numbers readily available in literature or quantifiable by testing. Hence the requirement for reliable experimental precipitation data.

The computational kinetic model was adjusted to match the experimental TTTs. The adjustment was developed by inputting the nucleation sites and interfacial energies to match the experiments' temperature and precipitation time at the nose of the TTT curves. As a result, the experimental-adjusted kinetic model correctly estimated the precipitation volume, times, and temperatures at the maximum kinetics temperature, Fig. 7.

Wilson et al. [35] proposed an algorithm for CCT calculations from isothermal data. Acuna et al. [39] followed Wilson's approach using the additive rule to calculate sigma phase CCT curves from the adjusted CALPHAD-based calculated TTTs on HDSS filler metals. Excellent agreement between the computational model and the experimental data was obtained defining a threshold cooling rate of 4 °C/s for sigma phase

Table 4
Sigma phase JMAK kinetics coefficients obtained from experimental data and CALPHAD-based data.

Kinetic equation $f = 1 - e^{(-kt^n)}$	Eutectoid precipitation or interface-controlled growth (experimental data)		Diffusion-controlled growth (experimental data)		Eutectoid precipitation or interface-controlled growth (CALPHAD data)	
Temperature	n	k	n	k	n	k
775	2.60	1.78E-08	0.97	1.32E-04	3.54	9.16E-14
800	2.79	1.25E-08	0.81	6.49E-04	3.44	1.75E-12
825	2.53	7.77E-08	0.60	3.41E-03	3.36	2.30E-11
850	2.76	2.21E-07	0.49	7.60E-03	2.94	2.90E-09
875	2.17	7.99E-07	0.57	5.20E-03	2.55	6.70E-08
900	1.92	3.33E-06	0.74	1.99E-03	1.92	3.37E-06
925	1.66	1.20E-05	0.86	9.68E-04	1.53	2.33E-05
950	1.74	6.69E-06	0.88	7.54E-04	1.10	1.13E-04
975	2.06	9.44E-07	1.13	1.45E-04	0.92	1.49E-04
1000	2.23	2.56E-07	1.09	1.20E-04	N/A	N/A
Average	**2.25**	2.68E-06	**0.81**	2.10E-03	**2.23**	3.49E-05
Max	2.79	1.20E-05	1.13	7.60E-03	0.92	9.16E-14
Min	1.66	1.25E-08	0.49	1.20E-04	3.54	1.49E-04

formation. Only thermal histories with cooling rates lower than 4 °C/s would cause sigma phase precipitation in the HDSS filler metal.

11. Kinetics analytical calculations from the CALPHAD model

The analytical kinetics calculations presented before are effective when experimental data is available. However, one of the targets of developing a computational model is to reduce the amount of experiments required. Therefore, the JMAK analytical calculations were applied to the CALPHAD-based kinetics results. Also, the Integrated Computational Materials Engineering (ICME) approach becomes much easier if the phase transformation can be described through a set of equations.

The developed sigma phase kinetics computational model is limited, in this paper, to TTTs from 1% to 10% volumetric fraction. This limitation is related to the CALPHAD model limitations of nucleation and not long-range diffusion. The linearized plots from Eq. (3) presented good linear regressions, Fig. 9 (a). However, the kinetic mechanism change seen before, Fig. 8, did not appear. The change in the kinetics mechanism is expected at a higher volumetric fraction, likely due to the exhaustion of nucleation sites.

Since the CALPHAD-based kinetics model is nucleation driven and its model-experimental adjustment fits the data up to 10% σ volume, the single kinetic behavior is consistent with the model used. The CALPHAD-based kinetics Avrami's exponent n values varied from 3.54 at the lower modeled temperature (775 °C) to 0.92 at the highest temperature (975 °C). Nevertheless, the calculated average n value was 2.23, in agreement with the value previously calculated from the experimental data (2.25), meaning a similar average transformation rate in both calculations, Table 4.

It is important to notice that n and k are different for each kinetic mechanism. While n does present some temperature dependency is not as significative as for k, which varies in orders of magnitude. The Avrami's exponent average has been used as a constant n by multiple authors [17–19,34,47]. The JMAK coefficients obtained from the CALPHAD-based kinetics data present an average n similar to the experimental interface-controlled growth kinetic mechanism. However, the activation energy coefficient k is highly temperature-dependent but also dependent on the n value. That relation caused the values to vary multiple orders of magnitude in each temperature regression. Close to the temperature range of maximum kinetics, between 875 °C and 925 °C, the analytical JMAK calculations from the experimental data and the CALPHAD calculations presented a reasonable agreement. However, at temperatures where the CALPHAD-based kinetics data describes reduced kinetics, either at higher or lower temperatures, the calculation and experimental values differ by one order of magnitude, Fig. 9 (b).

The k divergence observed is related to the shape of the CALPHAD-modeled TTTs, Fig. 7, where an excellent agreement was obtained for the nose of the curves, where kinetics is at maximum, 875 °C to 925 °C. However, the experimental data had a more comprehensive precipitation temperature range than the CALPHAD-based calculations. Meaning that at higher and lower temperatures, the size C curves do not present the same excellent agreement. This difference propagates to the JMAK calculations causing the divergence seen in Fig. 9 and Fig. 10. Nevertheless, the JMAK approach used in both datasets, experimental and CALPHAD-based TTTs, presented a good description of the sigma phase kinetics formation at the most critical temperature range, 875 °C to 925 °C, Fig. 10. Obtaining a single equation for the sigma phase kinetics precipitation is extremely valuable for implementing it as an ICME approach to connect models. With the obtained equations and the k array, sigma phase volume and possibly the inherent properties such as hardness and toughness can be predicted as a function of the thermal history imposed. This achievement is precious for manufacturing processes such as welding.

12. Conclusions

The kinetics of sigma phase formation of HDSS material has not received much research. We used controlled precipitation experiments to develop data on sigma phase kinetics in the HDSS filler metals. The kinetics of the sigma phase formation was addressed using the JMAK analytical calculations on experimental precipitation TTT data, and CALPHAD-based calculated TTTs. The modeled kinetics adequately described the sigma phase formation susceptibility in hyper duplex stainless steel welding filler metal. From the results obtained, the following conclusions were made.

1. High-quality experimental sigma phase precipitation data was obtained through physical simulation. These experimental Sigma phase TTT maps produced an adjusted CALPHAD-based kinetics TTT model. Which remarkably agreed with the experimental data up to $10\%_{vol}$ sigma phase.
2. The initial sigma phase precipitation occurred mainly at γ/α interfaces and at grain edges. The formed sigma morphologies suggested ferrite decomposition ($\alpha \rightarrow \sigma + \gamma_2$), presenting sigma and secondary austenite. Lamellar-like morphology cells were mainly seen in longer times, diffusion-controlled kinetics, at temperatures below 950 °C. Conversely, at temperatures beyond 950 °C, mainly blocky sigma phase grains were formed consuming the ferrite from one γ/α interface to the other.
3. A double-stage kinetics mechanism was identified for sigma phase formation:
   i. Eutectoid precipitation and interfacial-controlled growth, occurring until 250 s.
   ii. Diffusion-controlled growth, occurring after 250 s.

4. In the first kinetic stage, Avrami's exponent *n* suggests sigma phase precipitation characterized by grain edge nucleation and interfaced-controlled growth.
5. The Avrami's exponent *n* of the second kinetics stage, 0.81, suggests a diffusion-controlled growth with the thickening of plate-like grains.
6. Although the kinetics mechanism change is expected to be related to the formed phase volume, in our experiments, it occurred consistently at 250 s in the tested temperature ranges 775 °C - 1000 °C.
7. The JMAK approach using the CALPHAD-based TTT produced a good precipitation estimation close to maximum kinetics 875 °C to 925 °C. At higher temperatures, the calculations diverged by one order of magnitude.

Declaration of Competing Interest

The authors declare the following financial interests/personal relationships which may be considered as potential competing interests:

Andres Acuna reports financial support was provided by Manufacturing and Materials Joining Innovation Center.

Data availability

The raw/processed data required to reproduce these findings cannot be shared at this time as the data also forms part of an ongoing study.

Acknowledgments

The authors thank the Center for Electron Microscopy and Analysis (CEMAS) for its support in microscopy. NSF for the financial support through the IUCRC Program Award Numbers 1539992, 1822144, and 2052747 through the Manufacturing and Materials Joining Innovation Center (Ma^2JIC), and of Dr. Eric Brizes for the support and reference on the kinetics approach.

References

[1] K. Lorenz, G. Medawar, Thyssenforschung 1 (1969) 97–108.
[2] J.E. Truman, M.J. Coleman, K.R. Pirt, Br. Corros. J. 12 (1977) 236–238.
[3] S. Bernhardsson, In Duplex Stainless Steels '91, eds. J. Charles and S. Bernhardsson, Les Editions de Physique, France, 1991, pp. 185–210.
[4] A. P. I. API, API Publishing Services, 1220 L Street, NW, Washington, DC 20005, 2016, p. 38.
[5] B.B. Zhang, H.B. Li, S.C. Zhang, Z.H. Jiang, Y. Lin, H. Feng, H.C. Zhu, Mater. Charact. (2021) 175.
[6] J.O. Nilsson, Mater. Sci. Technol. 8 (1992) 685–700.
[7] L. Sun, Y.T. Sun, C.X. Lv, Y.Y. Liu, N.A.W. Dai, Y.M. Jiang, J. Li, D.D. Macdonald, Corros. Sci. (2021) 185.
[8] L. Sun, Y.T. Sun, Y.Y. Liu, N.W. Dai, J. Li, Y.M. Jiang, Mater. Corros. Werkstoffe Und Korrosion 70 (2019) 1682–1692.
[9] J.O. Nilsson, P. Kangas, T. Karlsson, A. Wilson, Metall. Mater. Trans. A Phys. Metall. Mater. Sci. 31 (2000) 35–45.
[10] C.-C. Hsieh, ISRN Metall. 2012 (2012) 1–16.
[11] E.O. Hall, S.H. Algie, J. Inst. Met. 94 (1966) 61.
[12] M. Avrami, J. Chem. Phys. 7 (1939) 1103–1112.
[13] M. Avrami, J. Chem. Phys. 2 (1940) 212.
[14] M. Avrami, J. Chem. Phys. 9 (1941) 177–184.
[15] W.A. Johnson, R.F. Mehl, Trans. Am. Inst. Min. Metall. Eng. 135 (1939) 416–442.
[16] A. Kolmogorov, Isvestiia Academii Nauk SSSR - Seriia Matematicheskaia 1 (1937) 333–359.
[17] J.W. Elmer, T.A. Palmer, E.D. Specht, Metall. Mater. Trans. A Phys. Metall. Mater. Sci. 38A (2007) 464–475.
[18] D.C. Dos Santos, R. Magnabosco, Metall. Mater. Trans. A Phys. Metall. Mater. Sci. 47A (2016) 1554–1565.
[19] I.J. Marques, A.D.A. Vicente, J.A.S. Tenorio, T.F.D. Santos, Mater. Res. Ibero Am. J. Mater. 20 (2017) 152–158.
[20] G. Chai, P. Kangas, 21st European Conference on Fracture, (Ecf21) 2, 2016, pp. 1755–1762.
[21] S.H. Jeon, S.T. Kim, I.S. Lee, J.S. Kim, K.T. Kim, Y.S. Park, Corros. Sci. 66 (2013) 217–224.
[22] S.H. Jeon, I.J. Park, H.J. Kim, S.T. Kim, Y.K. Lee, Y.S. Park, Mater. Trans. 55 (2014) 971–977.
[23] S.H. Jeon, S.T. Kim, I.S. Lee, J.S. Kim, K.T. Kim, Y.S. Park, J. Alloys Compd. 544 (2012) 166–172.
[24] S.H. Jeon, D.H. Hur, H.J. Kim, Y.S. Park, Corros. Sci. 90 (2015) 313–322.
[25] S.M. Kim, J.S. Kim, K.T. Kim, K.-T. Park, C.S. Lee, Mater. Sci. Eng. A 573 (2013) 27–36.
[26] S.-H. Jeon, H.-J. Kim, Y.-S. Park, Corros. Sci. 87 (2014) 1–5.
[27] B.B. Zhang, Z.H. Jiang, H.B. Li, S.C. Zhang, H. Feng, H. Li, Mater. Charact. 129 (2017) 31–39.
[28] M.L. Stein, Interpolation of Spatial Data: Some Theory for Kriging, Springer Science & Business Media, 1999.
[29] A.J. Ramirez, J.C. Lippold, S.D. Brandi, Metall. Mater. Trans. A Phys. Metall. Mater. Sci. 34A (2003) 1575–1597.
[30] A.J. Ramirez, S.D. Brandi, J.C. Lippold, Sci. Technol. Weld. Join. 9 (2004) 301–313.
[31] B. Josefsson, J.-O. Nillson, A. Wilson, In Duplex Stainless Steels '91, ed. J. Charles, Les Édition de Physique, Les Ulis, France, 1991, pp. 67–78.
[32] G.S. da Fonseca, P.S.N. Mendes, A.C.M. Silva, Metals (2019) 9.
[33] P. Ferro, F. Bonollo, G. Timelli, Metallurgia Italiana (2012) 7–12.
[34] R. Magnabosco, Mater. Res. Ibero Am. J. Mater. 12 (2009) 321–327.
[35] A. Wilson, J.O. Nilsson, Scand. J. Metall. 25 (1996) 178–185.
[36] R. Wagner, R. Kampmann, P. Voorhees, Phase Transformations in Materials, ed. G. Kostorz, Wiley-VCH, Weinheim, New York ; Chichester, 2001, p. ix, 713 pages.
[37] K.C. Russell, Adv. Colloid Interf. Sci. 13 (1980) 205–318.
[38] D. Kashchiev, Nucleation: Basic Theory with Applications, Butterworth Heinemann, Oxford; Boston, 2000.
[39] A. Acuna, A. Ramirez, R. Menon, P.-Å. Björnstedt, L. Carvalho, In ASME 2021 Pressure Vessels & Piping Conference, 2021.
[40] V. Hosseini, Materialia 98 (2019) 88–97.
[41] S.H. Byun, N. Kang, T.H. Lee, S.K. Ahn, H. Lee, W.S. Chang, K.M. Cho, Met. Mater. Int. 18 (2012) 201–207.
[42] G. Chail, P. Kangas, 21st European Conference on Fracture, (Ecf21) 2, 2016, pp. 1755–1762.
[43] W. Zhang, T. DebRoy, T.A. Palmer, J.W. Elmer, Acta Mater. 53 (2005) 4441–4453.
[44] J. Li, Z.H. Ma, X.S. Xiao, J.L. Zhao, L.Z. Jiang, Mater. Des. 32 (2011) 2199–2205.
[45] V. A. Hosseini, S. Wessman, K. Hurtig and L. Karlsson, 2016, pp. 88–97.
[46] G.S. da Fonseca, P.M. de Oliveira, M.G. Diniz, D.V. Bubnoff, J.A. de Castro, Mater. Res. Ibero Am. J. Mater. 20 (2017) 249–255.
[47] J.W. Christian, The Theory of Transformations in Metals and Alloys, Pergamon, Amsterdam ; Boston, 2002.